Metal-semiconductor-metal photodetectors based on graphene/*p*-type silicon Schottky junctions

Yanbin An,[1,a)] Ashkan Behnam,[2,a)] Eric Pop,[2,3] and Ant Ural[1,b)]

[1]*Department of Electrical and Computer Engineering, University of Florida, Gainesville, Florida 32611, USA*
[2]*Department of Electrical and Computer Engineering, Micro and Nanotechnology Lab,*
University of Illinois at Urbana-Champaign, Urbana, Illinois 61801, USA
[3]*Beckman Institute, University of Illinois at Urbana-Champaign, Urbana, Illinois 61801, USA*

Metal-semiconductor-metal (MSM) photodetectors based on graphene/*p*-type Si Schottky junctions are fabricated and characterized. Thermionic emission dominates the transport across the junctions above 260 K with a zero-bias barrier height of 0.48 eV. The reverse-bias dependence of the barrier height is found to result mostly from the Fermi level shift in graphene. MSM photodetectors exhibit a responsivity of 0.11 A/W and a normalized photocurrent-to-dark current ratio of $4.55 \times 10^4 \, \mathrm{mW^{-1}}$, which are larger than those previously obtained for similar detectors based on carbon nanotubes. These results are important for the integration of transparent, conductive graphene electrodes into existing silicon technologies. © *2013 American Institute of Physics*.
[http://dx.doi.org/10.1063/1.4773992]

The good electrical conductivity, high optical transparency, mechanical flexibility, and two-dimensional (2D) structure of graphene make it a promising candidate for transparent and conductive electrodes.[1–3] In the recent studies, it has been shown that graphene forms a Schottky junction with conventional semiconductors such as GaAs,[4] SiC,[4,5] GaN,[4,6] and Si.[4,7–9] In particular, there has been a growing interest in electronic and optoelectronic applications of graphene-silicon Schottky junctions, such as barristors[8] and solar cells based on graphene/bulk silicon[9,10] and graphene/silicon nanowire[11–13] junctions. Unlike conventional metal electrodes, graphene has the advantage that its Fermi level and hence workfunction can be tailored by chemical doping[14] or electrostatic gating.[15] This property has been utilized recently in device applications such as high efficiency chemically doped solar cells[9] and gate-controlled variable Schottky barrier devices.[8]

Most studies so far have extracted the Schottky barrier height Φ_B from room temperature *I-V* measurements. Temperature dependent *I-V* measurements, on the other hand, would enable the determination of barrier height without any assumptions of the electrically active area or the presence of any interfacial layer.[16,17] In addition, in contrast to solar cells, photodetector applications using graphene electrodes are much less explored, and most reports have focused on graphene junctions with *n*-type Si; *p*-type Si has been much less studied.

In this letter, we fabricate and characterize metal-semiconductor-metal (MSM) photodetectors where chemical vapor deposition (CVD)-grown monolayer graphene plays the role of the metal and the semiconductor is *p*-type silicon (*p*-Si). In order to understand the operation of these MSM photodetectors, we first investigate the electronic properties of graphene/*p*-Si Schottky junctions using metal-semiconductor (MS) structures as a function of temperature. With temperature-dependent *I-V* measurements, we also investigate the reverse-bias dependence of the Schottky barrier height. Finally, we characterize the photoresponse of interdigitated finger MSM photodetectors based on graphene/*p*-Si Schottky junctions. Our results provide important insights for the future integration of graphene based materials into existing semiconductor technologies.

Figure 1 shows a schematic of the fabrication process flow for the graphene/*p*-Si MSM photodetectors. A 1 mil copper foil (~25 μm thick, 99.8% pure) was first cleaned and annealed at 1000 °C in a CVD chamber. Graphene was then grown on the foil at the same temperature under the flow of 100 sccm CH$_4$ and 50 sccm H$_2$ at a pressure of 400 mTorr (Refs. 2, 3, 18, and 19) [Fig. 1(a)]. After growth, poly(methyl methacrylate) (PMMA) was deposited on top of graphene, followed by etching of the copper foil in FeCl$_3$ [Fig. 1(b)]. Si substrates with a *p*-type doping of $\sim 3 \times 10^{16} \, \mathrm{cm^{-3}}$ and a 300 nm thermally grown SiO$_2$ layer on top were cleaned [Fig. 1(c)] and windows were opened in the oxide layer [Fig. 1(d)]. Graphene was then transferred onto the patterned Si/SiO$_2$ substrates and the PMMA layer was removed. The Raman spectrum of graphene transferred onto SiO$_2$ measured at a laser wavelength of 632 nm is shown in Fig. 1(f), depicting the locations and relative intensities of the D, G, and 2D peaks. The strong G peak and the weak D peak indicate good graphitic quality, and the large 2D to G peak intensity ratio ($I_{2D}/I_G > 2$) confirm the monolayer nature of the CVD-grown graphene.[20,21] The full width at half maximum (FWHM) of the G, 2D, and D peaks for the transferred graphene calculated from Fig. 1(f) are 17.7, 35.3, and 14.8 cm^{-1}, respectively, which are in good agreement with the values reported in the previous studies on monolayer graphene.[15,22,23] Furthermore, we found that the Raman spectrum does not change significantly after device fabrication in the center of the patterned fingers. Only at the edges of the fingers, a larger D-peak is observed due to the presence of edge defects and dangling bonds, consistent with the previous Raman studies on patterned graphene nanoribbons.[24–26]

---

a)Y. An and A. Behnam contributed equally to this work.
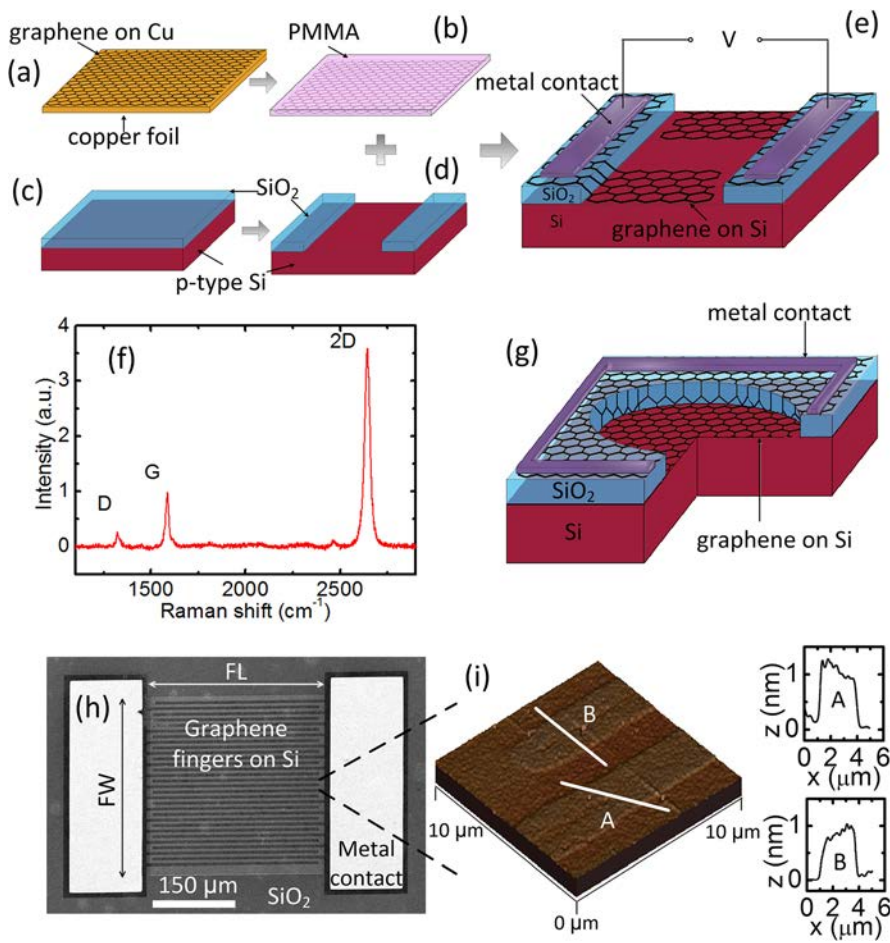b)Author to whom correspondence should be addressed. Electronic mail: antural@ufl.edu.

FIG. 1. Schematic of the fabrication process flow for the graphene/p-type Si MSM photodetectors: (a) Graphene is grown on a copper foil, (b) PMMA is deposited on top of graphene as a support layer followed by etching of the copper foil, (c) p-type Si substrates with thermally grown SiO_2 layers are cleaned, (d) windows are opened in the oxide layer, and (e) graphene is transferred onto the fabricated Si/SiO$_2$ substrate, the PMMA layer is removed, and graphene is patterned into interdigitated fingers. Ti/Au (5 nm/50 nm) metal contacts are patterned on the graphene areas lying on SiO$_2$ for electrical probing and wire bonding. (f) The Raman spectrum of graphene transferred onto SiO$_2$ measured at a laser wavelength of 632 nm depicting the locations and relative intensities of the D, G, and 2D peaks. (g) Schematic of a graphene/p-type Si MS junction that is fabricated using the same process flow as the MSM devices. (h) SEM image of a fabricated graphene/p-type Si MSM device with finger width $W = 5\,\mu m$, finger spacing $S = 5\,\mu m$, active area feature length $FL = 300\,\mu m$, and active area feature width $FW = 300\,\mu m$. (i) AFM image of patterned graphene fingers on Si, where the cross-sectional height profiles over the fingers labeled "A" and "B" are also depicted on the right. "x" denotes distance and "z" denotes height over the fingers.

Measured Raman maps on different locations of the transferred graphene show that more than 80% of the graphene is monolayer.

After graphene was transferred onto the Si/SiO$_2$ substrate, it was patterned by plasma etching[27] into graphene/p-Si MSM structures consisting of graphene interdigitated finger electrodes [Fig. 1(e)], as well as graphene/p-Si MS junctions [Fig. 1(g)]. Finally, Ti/Au (5 nm/50 nm) metal contacts were patterned on the graphene areas lying on SiO$_2$ for electrical probing and wire bonding. Figure 1(h) shows a scanning electron microscopy (SEM) image of a finished graphene/p-Si MSM device. Atomic force microscope (AFM) image of patterned graphene fingers on Si is shown in Fig. 1(i).

We first characterize the temperature-dependent I-V behavior of graphene/p-Si MS structures in order to extract the Schottky barrier height Φ_B.[16] Figure 2(a) shows the semi-log I-V characteristics of the graphene/p-Si MS junction at temperatures ranging from 260 to 380 K. The device has rectifying I-V characteristics, confirming the Schottky nature of the junction between graphene and p-Si. A magnified view of the low forward-bias region in the same temperature range is shown in the upper inset of Fig. 2(a), where the temperature-dependent exponential slopes are visible. The temperature dependence of the low forward-bias current and the reverse saturation current suggests that the electronic transport in the graphene/p-Si junction is dominated by thermionic emission at temperatures above 260 K,[17,28] which is expressed by

$$I = AA^{**}T^2 \exp\left(-\frac{\Phi_B}{kT}\right)\left[\exp\left(\frac{qV}{nkT}\right) - 1\right], \qquad (1)$$

where A is the effective junction area, A^{**} is the reduced effective Richardson constant, T is absolute temperature, Φ_B is the Schottky barrier height between graphene and p-Si (in units of eV), k is the Boltzmann constant, q is the electronic charge, and n is the ideality factor. Note that in Eq. (1), the series resistance term is ignored since our analysis is based on reverse current only, where the contribution from the series resistance is negligible. The lower inset of Fig. 2(a) shows the Arrhenius plot of the reverse saturation current at a reverse bias of 2 V. As we can see from the figure, at higher temperatures, the current becomes strongly dependent on temperature; however, below 260 K, the temperature dependence is very weak, which suggests that tunneling through the Schottky barrier starts to dominate the electronic transport.[17]

The Schottky barrier height can be extracted from the slope of the Richardson plot (log I/T^2 vs. $1/T$) of the reverse saturation current in the temperature region dominated by thermionic emission, as shown in Fig. 2(b).[17,28] The figure shows the Richardson plot at a reverse bias of 2 V and the linear best-fit, from which the barrier height Φ_B is extracted to be 0.46 eV. Furthermore, by performing the barrier height extraction at various reverse bias values in the saturation region, the reverse bias dependence of the Schottky barrier height can be obtained, as shown in Fig. 2(c).

There are two main factors which could contribute to the reverse bias dependence of the Schottky barrier height.
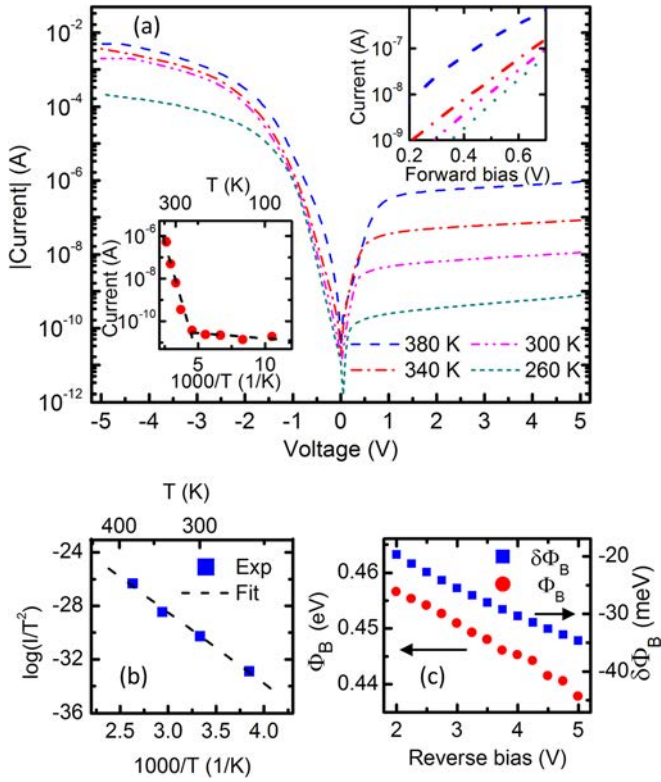
FIG. 2. (a) Current-voltage characteristics for a graphene/*p*-Si Schottky junction with $2.5 \times 10^5 \, \mu m^2$ area at various temperatures ranging from 260 K to 380 K. The upper inset depicts a magnified view of the low forward-bias region of the same *I-V* characteristics as in the main panel. The lower inset is an Arrhenius plot of the reverse saturation current at 2 V bias in the temperature range 95 K to 380 K for the same device as in the main panel, which shows the transition from thermionic emission to tunneling transport. (b) The experimental Richardson plot (log I/T^2 vs. $1/T$) for the device in part (a) at a reverse bias of 2 V in the thermionic emission dominated temperature region and the linear best-fit, which yields the Schottky barrier height. (c) The experimentally extracted Schottky barrier height Φ_B (left *y*-axis) and the calculated change in the Schottky barrier height due to the Fermi level shift in graphene $\delta\Phi_B$ (right *y*-axis) as a function of reverse bias V_R for the same device as in part (a). Note that the two curves exhibit relatively similar slopes.

The first is image-force barrier lowering and the second is Fermi level and hence workfunction changes in metals with low density of states due to charge transfer from Si. Our as-prepared, isolated graphene (i.e., before the junction is formed with silicon) is *p*-type with an estimated carrier (i.e., hole) concentration of $n_0 \approx 3.5 \times 10^{12} \, cm^{-2}$ based on gate-dependent measurements of graphene field effect transistor (FET) structures fabricated on the same chip together with the MSM structures. The Fermi level shift in graphene (E_F) relative to the Dirac point (where $E_F = 0$) due to this extrinsic doping is given approximately by[29]

$$E_F = -\text{sgn}(n_0)\hbar v_F \sqrt{\pi|n_0|}, \qquad (2)$$

where $\hbar$ is the reduced Planck constant, $\nu_F = 1.1 \times 10^8$ cm/s is the Fermi velocity of graphene, and the carrier concentration n_0 is defined to be positive for holes and negative for electrons. Once the graphene/*p*-Si junction is formed, a space charge Q_s (per unit area) forms in the depletion region of Si given under the depletion approximation by

$$Q_s = -qN_A x_d = -\sqrt{2q\varepsilon_s N_A(V_{bi} + V_R)}, \qquad (3)$$

where N_A is the acceptor density, x_d is the depletion region width, ε_s is the permittivity of silicon, V_{bi} is the built-in voltage, and V_R is the magnitude of reverse bias. V_{bi} is given by $qV_{bi} = \Phi_B^0 - (E_{F,Si} - E_V)$, where Φ_B^0 is the zero-bias barrier height, and $E_{F,Si}$ and E_V denote the Fermi level and the valence band of Si, respectively, as shown in the thermal equilibrium band diagram of Fig. 3(a). Neglecting any interface state charges, an equal and opposite charge Q_G develops on the graphene side, i.e., $Q_G = -Q_s$. This charge induces additional holes and makes the new carrier density n in graphene $n = n_0 + Q_G/q$, neglecting any thermally generated carriers. Replacing n_0 in Eq. (2) with this new n, and using the expression for Q_s in Eq. (3), the total Fermi level shift in graphene relative to the Dirac point now becomes reverse-bias dependent, i.e.,

$$E_F(V_R) = -\hbar v_F \sqrt{\pi\left(|n_0| + \sqrt{2\varepsilon_s N_A(V_{bi} + V_R)/q}\right)}. \qquad (4)$$

The expression in Eq. (4) includes the Fermi level shift due to extrinsic doping, thermal equilibrium contact with Si, and reverse bias. Assuming an ideal Schottky junction where surface-state effects are neglected, the corresponding change $\delta\Phi_B$ in the Schottky barrier height due to the Fermi level shift in graphene with reverse bias is then given by

$$\delta\Phi_B(V_R) \equiv \Phi_B(V_R) - \Phi_B^0 = E_F(V_R) - E_F^0, \qquad (5)$$

where E_F^0 is the zero-bias graphene Fermi-level shift [i.e., $E_F(V_R = 0)$]. Note that, in the case of a graphene junction with *p*-Si, the decrease in E_F of graphene with increasing reverse bias decreases Φ_B as shown in Fig. 3(b), i.e., $\delta\Phi_B$ is negative. The opposite would be true for *n*-type Si.

We can calculate and plot $\delta\Phi_B$ as a function of V_R using Eqs. (4) and (5), as shown in Fig. 2(c) along with the experimental Φ_B vs. V_R curve. Since V_{bi} in Eq. (4) depends on Φ_B^0, a self-consistent calculation was performed by iteration in order to find V_{bi}. Since $\delta\Phi_B$ vs. V_R and Φ_B vs. V_R curves in Fig. 2(c) exhibit relatively similar slopes, we can conclude that most of the contribution to the reverse bias dependence of Φ_B comes from the Fermi level shift in graphene.
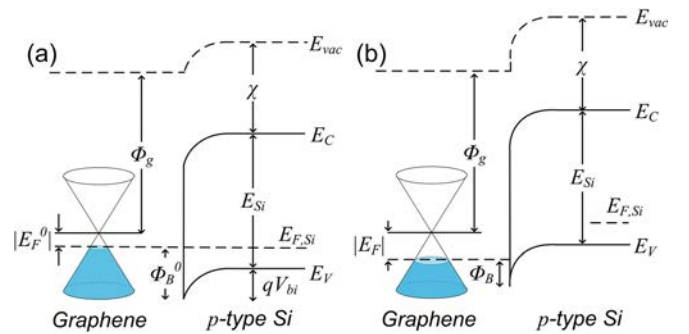

FIG. 3. Energy band diagram of the graphene/*p*-Si Schottky junction (a) at thermal equilibrium and (b) under reverse bias V_R. E_{vac} is the vacuum level, χ, E_C, E_{Si}, $E_{F,Si}$, and E_V are the electron affinity, conduction band, bandgap, Fermi level, and valence band of Si, respectively. Furthermore, V_{bi} is the built-in voltage, Φ_g is the workfunction of intrinsic graphene, E_F is the graphene Fermi-level shift, and Φ_B is the Schottky barrier height. The superscripts "0" in part (a) denote thermal equilibrium (i.e., zero-bias) values. Note that the graphene Fermi level shifts further down relative to the Dirac point under reverse bias, decreasing Φ_B.

Furthermore, the slightly larger slope of the Φ_B vs. V_R curve indicates that there could also be a contribution from image-force barrier lowering. This is different from Schottky junctions with conventional metals in which the Fermi level is fixed and the reverse bias dependence of barrier height is primarily due to image force lowering.[17] Extrapolating the experimental data to zero-bias using Eqs. (4) and (5), we obtain $E_F^0 = -0.25$ eV and a zero-bias barrier height of $\Phi_B^0 = 0.48$ eV. Furthermore, the workfunction of intrinsic (i.e., $E_F = 0$) graphene Φ_g can be calculated from $\Phi_g + |E_F^0| + \Phi_B^0 = \chi + E_{Si}$, where χ and E_{Si} are the electron affinity and band gap, respectively, of Si, as shown in Fig. 3. By using the extracted values of E_F^0 and Φ_B^0, we obtain $\Phi_g = 4.45$ eV, which is in good agreement with the values reported in the literature.[30] Previous studies have suggested that charge puddles could form after transferring graphene onto SiO_2 substrates.[31,32] The presence of charge puddles locally induces different doping levels in graphene, resulting in a distribution of barrier heights and Schottky barrier inhomogeneities.[5,9] Therefore, the extracted barrier height is an "effective" value over the contact area.

With the extracted Schottky barrier height, we find that the calculated reverse saturation current levels from Eq. (1) are significantly higher than the experimental data. This difference in the measured and calculated current levels could be explained by the presence of a thin interfacial native oxide layer between graphene and Si, which lowers the current by introducing quantum tunneling.[33] The interfacial native oxide layer could grow during the time between the etching of the thermal oxide and the graphene transfer as the Si substrate is exposed to air. We found that devices fabricated with an additional HF cleaning step immediately prior to graphene transfer also exhibited this lower current, indicating that the native oxide could also grow during the graphene transfer process since it involves wet chemical processing in H_2O. Another possibility is that oxygen molecules could diffuse through holes or cracks in the graphene after deposition and form the native oxide at the silicon surface. Recently, it was shown that a native oxide layer is beneficial to the performance of graphene/Si Schottky junction solar cells, which was attributed to surface passivation effects.[9] In the case of MSM photodetectors, the interfacial native oxide layer acts as a tunnel barrier and helps reduce the dark current and increase the sensitivity. An interfacial oxide layer has been intentionally introduced previously in conventional Aluminum-Silicon MSM photodetectors to minimize the dark current.[34]

The effect of carrier tunneling through the thin interfacial oxide layer can be incorporated into Eq. (1) as an exponential prefactor $\exp(-\gamma^{0.5}\delta_t)$, where δ_t is the thickness of the thin native oxide layer and γ is the effective tunneling barrier height of the oxide (which also depends on δ_t) as[33]

$$I = AA^{**}T^2 \exp(-\gamma^{0.5}\delta_t)\exp\left(-\frac{\Phi_B}{kT}\right)\left[\exp\left(\frac{qV}{nkT}\right) - 1\right]. \quad (6)$$

By comparing the experimental and theoretically calculated current values, the tunneling factor is estimated as $\gamma^{0.5}\delta_t \approx 8.23-8.95$ eV$^{0.5}$ Å depending on the reverse bias chosen, corresponding to an oxide thickness δ_t between 1.9 and 2.6 nm.[33] It is worth noting that extracting Φ_B using the

Richardson plot was critical in obtaining the value of $\gamma^{0.5}\delta_t$ since values of Φ_B and $\gamma^{0.5}\delta_t$ cannot be obtained independently at a fixed temperature.

After the analysis of the electronic properties of reverse-biased graphene/p-Si junctions, we turn to characterize the device performance of graphene/p-Si/graphene MSM photodetectors based on these junctions. The inset of Fig. 4 shows the dark I-V characteristics at room temperature for the graphene/p-Si MSM structure in the bias range from -3 V to 3 V, which shows the typical characteristics expected for two back-to-back Schottky diodes. The dark I-V characteristics in the figure are symmetric, suggesting that the Schottky junctions formed at different graphene fingers are uniform.

To characterize the photoresponse of the graphene/p-Si MSM photodetectors, they were illuminated with a He-Ne laser (633 nm wavelength, 5.1 mW power, and $\sim$830 μm spot size) at room temperature. The main panel of Fig. 4 shows the dark and photocurrent of the same MSM device as in the inset as a function of voltage bias up to 5 V. As we can see from the figure, the device current increases by close to five orders of magnitude at 5 V bias under laser illumination. An important performance metric for MSM photodetectors is the normalized photocurrent-to-dark current ratio (NPDR) defined as[35,36]

$$NPDR = (I_{photo}/I_{dark})/P_{inc} = \Re/I_{dark}, \quad (7)$$

where I_{photo} and I_{dark} are the photo and dark current, respectively, P_{inc} is the incident optical power, and $\Re$ is the responsivity given by $\Re = I_{photo}/P_{inc}$. Responsivity and NPDR values at 5 V are 0.11 A/W and 4.55×10^4 mW^{-1}, respectively. This NPDR value is larger than those reported for carbon nanotube film-Si MSM photodetectors due to the lower dark current.[37] It can also be observed in Fig. 4 that the photocurrent increases with increasing bias, which could be due to defects at the graphene/p-Si interface.[38]
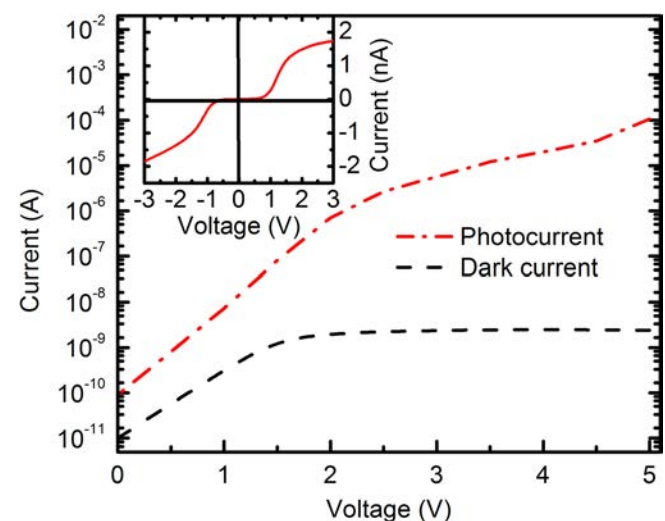

FIG. 4. Dark current and photocurrent as a function of bias voltage measured at room temperature for a graphene/p-Si MSM photodetector with finger width $W = 10$ μm, finger spacing $S = 10$ μm, active area feature length $FL = 400$ μm, and active area feature width $FW = 400$ μm. The photocurrent is measured under 633 nm He-Ne laser illumination with 5.1 mW power and $\sim$830 μm spot size. The inset shows the dark I-V characteristics for the same device as in the main panel.

It is also worth noting that the series resistances of the MSM devices do not limit the photocurrent even at the highest voltage bias measured. The contact resistance between the Ti/Au metal electrode and graphene dominates the total series resistance. Based on the contact resistivity obtained from four-point and two-point measurements of graphene patterned into four-point-probe structures, the series resistance of the device in the main panel of Fig. 4 is more than 20 times smaller than the measured MSM device resistance even under laser illumination at 5 V.

In conclusion, we fabricated and characterized CVD-grown monolayer graphene/p-Si MSM photodetectors as well as MS Schottky junctions. The reverse-bias dependence of the Schottky barrier height, which is extracted from Richardson plots, is found to result mainly from the Fermi level shift in graphene, with an extrapolated zero-bias barrier height of $\Phi_B^0 = 0.48$ eV. In addition, comparison of the experimental and theoretically calculated reverse saturation current values suggests the presence of a thin interfacial native oxide layer between graphene and Si. Finally, we studied the photoresponse of the MSM photodetectors under laser illumination and extracted the responsivity and NPDR values. Although further research is needed to understand and control the microscopic properties of the interface between graphene and Si, graphene holds promise as a transparent, conductive electrode that can be integrated with existing silicon technologies.

[1] K. S. Novoselov, A. K. Geim, S. V. Morozov, D. Jiang, Y. Zhang, S. V. Dubonos, I. V. Grigorieva, and A. A. Firsov, Science **306**, 666 (2004).

[2] K. S. Kim, Y. Zhao, H. Jang, S. Y. Lee, J. M. Kim, K. S. Kim, J.-H. Ahn, P. Kim, J.-Y. Choi, and B. H. Hong, Nature **457**, 706 (2009).

[3] R.-H. Kim, M.-H. Bae, D. G. Kim, H. Cheng, B. H. Kim, D.-H. Kim, M. Li, J. Wu, F. Du, H.-S. Kim, S. Kim, D. Estrada, S. W. Hong, Y. Huang, E. Pop, and J. A. Rogers, Nano Lett. **11**, 3881 (2011).

[4] S. Tongay, M. Lemaitre, X. Miao, B. Gila, B. R. Appleton, and A. F. Hebard, Phys. Rev. X **2**, 011002 (2012).

[5] S. Shivaraman, L. H. Herman, F. Rana, J. Park, and M. G. Spencer, Appl. Phys. Lett. **100**, 183112 (2012).

[6] H. Zhong, Z. Liu, G. Xu, Y. Fan, J. Wang, X. Zhang, L. Liu, K. Xu, and H. Yang, Appl. Phys. Lett. **100**, 122108 (2012).

[7] C.-C. Chen, M. Aykol, C.-C. Chang, A. F. J. Levi, and S. B. Cronin, Nano Lett. **11**, 1863 (2011).

[8] H. Yang, J. Heo, S. Park, H. J. Song, D. H. Seo, K.-E. Byun, P. Kim, I. Yoo, H.-J. Chung, and K. Kim, Science **336**, 1140 (2012).

[9] X. Miao, S. Tongay, M. K. Petterson, K. Berke, A. G. Rinzler, B. R. Appleton, and A. F. Hebard, Nano Lett. **12**, 2745 (2012).

[10] X. Li, H. Zhu, K. Wang, A. Cao, J. Wei, C. Li, Y. Jia, Z. Li, X. Li, and D. Wu, Adv. Mater. **22**, 2743 (2010).

[11] G. Fan, H. Zhu, K. Wang, J. Wei, X. Li, Q. Shu, N. Guo, and D. Wu, ACS Appl. Mater. Interfaces **3**, 721 (2011).

[12] T. Feng, D. Xie, Y. Lin, Y. Zang, T. Ren, R. Song, H. Zhao, H. Tian, X. Li, H. Zhu, and L. Liu, Appl. Phys. Lett. **99**, 233505 (2011).

[13] C. Xie, P. Lv, B. Nie, J. Jie, X. Zhang, Z. Wang, P. Jiang, Z. Hu, L. Luo, Z. Zhu, L. Wang, and C. Wu, Appl. Phys. Lett. **99**, 133113 (2011).

[14] Y. Shi, K. K. Kim, A. Reina, M. Hofmann, L.-J. Li, and J. Kong, ACS Nano **4**, 2689 (2010).

[15] A. Das, S. Pisana, B. Chakraborty, S. Piscanec, S. K. Saha, U. V. Waghmare, K. S. Novoselov, H. R. Krishnamurthy, A. K. Geim, A. C. Ferrari, and A. K. Sood, Nat. Nanotechnol. **3**, 210 (2008).

[16] A. Behnam, N. A. Radhakrishna, Z. Wu, and A. Ural, Appl. Phys. Lett. **97**, 233105 (2010).

[17] S. M. Sze, *Physics of Semiconductor Devices* (Wiley, 1981).

[18] S. Bae, H. Kim, Y. Lee, X. Xu, J.-S. Park, Y. Zheng, J. Balakrishnan, T. Lei, H. Ri Kim, Y. I. Song, Y.-J. Kim, K. S. Kim, B. Ozyilmaz, J.-H. Ahn, B. H. Hong, and S. Iijima, Nat. Nanotechnol. **5**, 574 (2010).

[19] J. D. Wood, S. W. Schmucker, A. S. Lyons, E. Pop, and J. W. Lyding, Nano Lett. **11**, 4547 (2011).

[20] A. C. Ferrari, J. C. Meyer, V. Scardaci, C. Casiraghi, M. Lazzeri, F. Mauri, S. Piscanec, D. Jiang, K. S. Novoselov, S. Roth, and A. K. Geim, Phys. Rev. Lett. **97**, 187401 (2006).

[21] Y. K. Koh, M.-H. Bae, D. G. Cahill, and E. Pop, ACS Nano **5**, 269 (2011).

[22] D. Graf, F. Molitor, K. Ensslin, C. Stampfer, A. Jungen, C. Hierold, and L. Wirtz, Nano Lett. **7**, 238 (2007).

[23] S. Pisana, M. Lazzeri, C. Casiraghi, K. S. Novoselov, A. K. Geim, A. C. Ferrari, and F. Mauri, Nature Mater. **6**, 198 (2007).

[24] D. Bischoff, J. Guttinger, S. Droscher, T. Ihn, K. Ensslin, and C. Stampfer, J. Appl. Phys. **109**, 073710 (2011).

[25] S. Ryu, J. Maultzsch, M. Y. Han, P. Kim, and L. E. Brus, ACS Nano **5**, 4123 (2011).

[26] A. Behnam, A. S. Lyons, M.-H. Bae, E. K. Chow, S. Islam, C. M. Neumann, and E. Pop, Nano Lett. **12**, 4424 (2012).

[27] A. Behnam, Y. Choi, L. Noriega, Z. Wu, I. Kravchenko, A. G. Rinzler, and A. Ural, J. Vac. Sci. Technol. B **25**, 348 (2007).

[28] D. K. Schroder, *Semiconductor Material and Device Characterization* (Wiley-Interscience, 1998).

[29] K. S. Novoselov, A. K. Geim, S. V. Morozov, D. Jiang, M. I. Katsnelson, I. V. Grigorieva, S. V. Dubonos, and A. A. Firsov, Nature **438**, 197 (2005).

[30] Y.-J. Yu, Y. Zhao, S. Ryu, L. E. Brus, K. S. Kim, and P. Kim, Nano Lett. **9**, 3430 (2009).

[31] Y. Zhang, V. W. Brar, C. Girit, A. Zettl, and M. F. Crommie, Nat. Phys. **5**, 722 (2009).

[32] A. Deshpande, W. Bao, F. Miao, C. N. Lau, and B. J. LeRoy, Phys. Rev. B **79**, 205411 (2009).

[33] H. C. Card and E. H. Rhoderick, J. Phys. D: Appl. Phys. **4**, 1589 (1971).

[34] M. Seto, C. Rochefort, S. D. Jager, R. F. M. Hendriks, G. W. T. Hooft, and M. B. V. D. Mark, Appl. Phys. Lett. **75**, 1976 (1999).

[35] C. O. Chui, A. K. Okyay, and K. C. Saraswat, IEEE Photonics Technol. Lett. **15**, 1585 (2003).

[36] A. Behnam, J. Johnson, Y. Choi, L. Noriega, M. G. Ertosun, Z. Wu, A. G. Rinzler, P. Kapur, K. C. Saraswat, and A. Ural, J. Appl. Phys. **103**, 114315 (2008).

[37] A. Behnam, J. L. Johnson, Y. Choi, M. G. Ertosun, A. K. Okyay, P. Kapur, K. C. Saraswat, and A. Ural, Appl. Phys. Lett. **92**, 243116 (2008).

[38] J. Burm and L. F. Eastman, IEEE Photonics Technol. Lett. **8**, 113 (1996).